lajss.org© Latin American Journal of Solids and Structures

www.lajss.org

Theoretical model based on configuration decomposition for the fragment velocity of the prism charge structure

Haokai Li[a], Yuxiang Feng[a], Yuan Li[a,b*], Tao Suo[a,b]

[a] School of Aeronautics and Institute of Extreme Mechanics, Northwestern Polytechnical University, Xi'an 710072, Shaanxi, China. Email: lihaokai@mail.nwpu.edu.cn; 570286905@qq.com; panshi@nwpu.edu.cn; suotao@nwpu.edu.cn

[b] National Key Laboratory of Strength and Structural Integrity, Xi'an 710072, Shaanxi, China

* Corresponding author

Abstract

The prism charge warhead can achieve a good balance between dense damage elements and reduced aiming time. However, the conventional fragment velocity theory can't be directly applied to calculate the fragment velocity of polygonal charges, resulting in a lack of effective metrics to evaluate their lethality and to guide practical design. In this study, the configuration decomposition method was first used to quantify the distribution relationship between polygonal charges and sandwich charges, and a preliminary model was established. Secondly, through numerical modeling, the unknown function within the model was determined, and pulsed X-ray experiments were designed and executed. Finally, the accuracy and applicability of the established model were verified using the test results, publicly published test results, and additional numerical simulations. The study's numerical simulations show high precision, with an absolute error of <5.44%. The error of the established calculation model is controlled within 7.70%. This research can provide a reliable tool for designing and optimizing the power of prism charge warheads.

Keywords

prism charge warhead; sandwich charge; configuration decomposition; pulsed X-ray experiment; fragment velocity model

Graphical Abstract

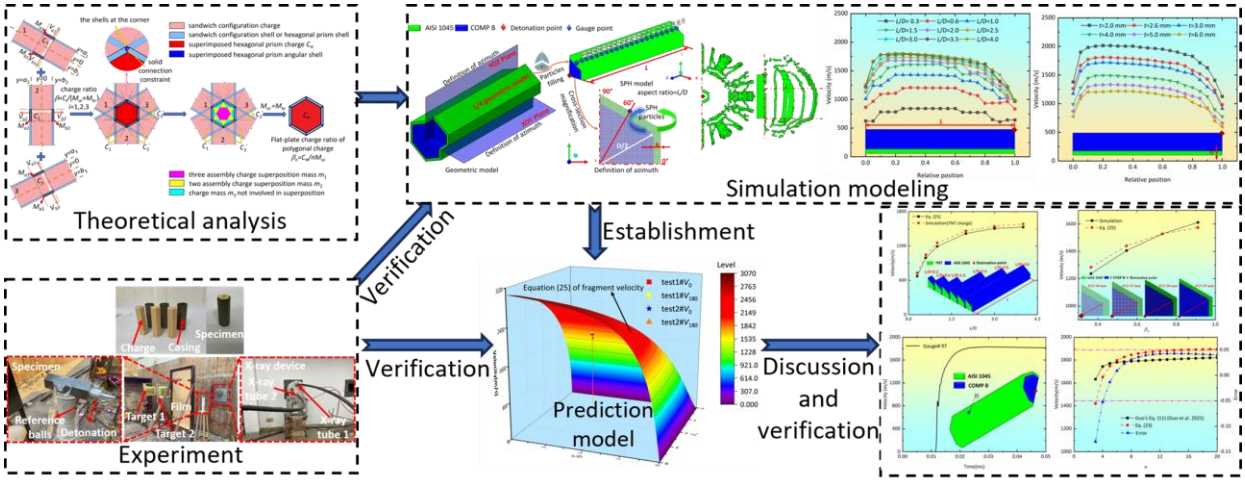

1 INTRODUCTION

Charge detonation driving is a crucial method for achieving high-velocity loading of fragments and other charge covers (Zhang et al. 2001; Wang 2019; Zhang et al. 2023). Efficient driving capability enables higher destructive power on targets, significantly enhancing the performance of weapons (Kennedy 1999; Deng et al. 2022a; Wang et al. 2016). Given the current limitations in explosive energy density (Hu and Xiao 2019), it is essential to explore alternative methods to boost the detonation-driving capability of explosives. One of the key approaches is the design of charge structures (Held 2001; Wang et al. 2022b). With the advancement of new hypersonic weapons, the need to adapt to the aerodynamic shapes of these weapons has made charge structural design a prominent research topic (Terry and Cone 2020; Wang et al. 2022a). Newly studied examples include double-layer structure (Hamada et al. 2004; Zhang et al. 2011; Ye et al. 2024), focus structure (Feng et al. 2009; Wang et al. 2023), developable structure (Zhao et al. 2016a, b), cone structure (Guo et al. 2018), hollow cylindrical structure (An et al. 2018; Li et al. 2023c), sector-shaped structure (Ling et al. 2017), charge shell mismatch structure (Dhote et al. 2015; Gao et al. 2020; Guo et al. 2023), prismatic structures (Cunard and Thomas 1992; Waggener 2001; Huang et al. 2023), D-shaped structures (Guo et al. 2019b, 2020), elliptical structures (Deng et al. 2022b, 2024, 2025), and drum-shaped structures (Li et al. 2024a). Among these special-shaped charge structures, prismatic and D-shaped designs incorporating flat plates can form dense, high-velocity fragment beams in the flat sections. This is mainly due to the advantage that the detonation-driven plate can form a dense fragment beam with a small flying angle, which is beneficial to the damage effect of the target (Resnyansky et al. 1999; Jin et al. 2004; Lim 2013; Ding et al. 2017). These structures demonstrate effective lethality against targets and have garnered significant attention.

However, the aforementioned special-shaped structures containing flat plates have limitations in certain aspects. The effective killing fragments of D-shaped charge structures are mainly produced in the flat part (Guo et al. 2019b, 2020), causing efficient damage to targets in only one direction, which requires a high velocity for the weapon steering device to aim. For prismatic structures, Ning et al. (2017) and Ma et al. (2020) conducted both experimental and numerical research on fragment dispersions of triangular prism charges with preformed fragments. To achieve efficient damage with the triangular prism aimable warhead, a certain rotation is needed to aim at the target. Similar to the D-shaped warhead, the triangular prism charge warhead also imposes high rotational velocity requirements on the weapon steering device. To reduce the aiming time of the fragment beam at the target, scholars have studied quadrangular and hexagonal prism charge warheads capable of producing multiple fragment beams. Boswell and Rueb (1999) invented a quadrangular prism charge warhead structure that can rotate along the axis of the charge. When detonated, one side of the charge is aimed at the target. Due to the increase in dense fragment beams, this structure is easier to aim at the target than the triangular prism charge warhead. Huang et al. (2023) established a quadrangular prism charge warhead and, based on numerical simulation results of different eccentric initiations, derived an equation for calculating the fragment velocity of the quadrangular prism charge warhead in four directions. However, the fitting effect of the equation at the circumferential positions was not ideal. Shi et al. (2023) designed a concave quadrilateral prism charge warhead with preformed spherical fragments based on the quadrangular prism charge warhead. Experimental results showed that the preformed fragments mainly produced dense perforation damage on the four planes of the octagonal target plate. This indicates that the quadrangular prism charge warhead can only produce dense fragment beams in four directions, limiting its coverage ability in the circumferential direction. To address this, Li and Wen (2014, 2017) and Li (2016) studied a hexagonal prism charge warhead capable of producing multiple fragment beams. Li and Wen (2014) and Li (2016) performed a comparative analysis of the hexagonal prism charge warhead with preformed fragments and the circular cross-section warhead with preformed fragments, concluding that the hexagonal prism charge warhead can generate dense fragment beams covering six directions. When the asymmetric 8-point detonation was initiated, a significant fragment-focusing effect was produced, and both fragment velocity and kinetic energy were significantly enhanced. The hexagonal prism charge warhead can form six dense high-energy fragment beams covering six directions, thereby achieving a good balance between dense damage elements and the reduction of aiming time. It is a prism structure with high fragmentation and explosive utilization efficiency.

Currently, most investigations of hexagonal-prism charge warheads focus on those incorporating preformed spherical fragments, with a predominant emphasis on detonation methods. A significant gap exists in the calculation methodology for fragment velocities of hexagonal prism charge warheads, hindering comprehensive power assessments and impeding practical design implementations. The fragment velocity of warheads with different charge structures is an important index to evaluate their damage power (Gurney 1943; Taylor 1963; Karpp and Predebon 1975; Huang et al. 2015). This deficiency underscores the pressing need to investigate the governing dynamics of fragment velocities

propelled by internal detonations within these warheads and to formulate a corresponding velocity computation equation.

To address this, we use the configuration decomposition method to decompose the prism charge into a combination of multiple basic sandwich charges. We return the theoretical model analysis of the fragment velocity of the prism charge to the basic sandwich charge analysis. Subsequently, based on the configuration decomposition method and the characteristics of the prism charge, we consider the influence of prismatic angular shell and constraint failure on the fragment velocity of disassembled sandwich charge, leading to a preliminary model for the fragment velocity of hexagonal prism charge warheads. Secondly, through numerical modeling, the unknown function within the model was determined, and subsequent improvements were made. To validate the accuracy of the derived model, pulsed X-ray experiments were designed and executed. Finally, the accuracy and applicability of the established model were verified using the test results, publicly published test results, and additional numerical simulations. To date, the superposition effect of prismatic charges has been discovered and validated, and subsequently applied to establish a fragment velocity calculation model for polygonal charges. This model, rigorously verified through multiple experimental and simulation datasets, demonstrates robust accuracy and applicability, representing novel aspects of this study. Unfortunately, this study only focuses on the calculation of fragment velocities of prism charges, and the lack of other minor parameters to evaluate the power of the charge is the main limitation of this study. These results can offer valuable insights for the design, research, and application of multi-faceted structural charge warheads.

2 FRAGMENT VELOCITY MODEL

2.1 Configuration decomposition

The hexagonal prism charge warhead is a multi-faceted and multi-angular charge structure. From the perspective of the sandwich charge for accelerating flyer plates, it can be decomposed as a combination composite of three symmetrical sandwich charges, labeled as 1, 2, and 3 in Figure 1 (a), each separated by an angle of 60°. Figure 1 shows the combination formation process of the hexagonal prism charge warhead. The charge inside the hexagonal prism is the combination of three sandwich charges; the shells of the hexagonal prism charge warhead are the shells of the three sandwich charges, and the shells at the corners are the combination of two adjacent sandwich charges, as shown in Figure 1 (b). However, since the charge mass of a single sandwich charge participates in the combination, this part of the mass does not all act on the plates of both sides of the charge, but is reduced instead due to allocation, as shown in Figure 1 (c). In addition, the shells at corners are formed on both sides of the three sandwich charge shells after combination and allocation, and the constraints are formed between the shells at corners, as shown in Figure 1 (b). Therefore, the Gurney equation for the sandwich charge for accelerating flyer plates (Jones et al. 1980) cannot be applied to the direct solution of the hexagonal prism charge warhead. We need to reanalyze the energy conservation of a single sandwich charge after combination and allocation. To this end, we first need to determine the charge mass of the sandwich charge after combination and allocation, and its relationship with the total mass of the hexagonal prism charge warhead.

From the perspective of configuration decomposition, the charge masses C_1, C_2, and C_3 of the sandwich charges No.1, 2, and 3 in Figure 1 (a) have been reduced, thereby transforming into C_1', C_2', and C_3' in the superimposed hexagonal prism charge warhead ($C_1 > C_1', C_2 > C_2', C_3 > C_3'$). C_1', C_2', and C_3' together constitute the total charge mass C_H of the hexagonal prism charge warhead.

$$C_H = C_1^{'} + C_2^{'} + C_3^{'} = m_1 + 6m_2 + 6m_3 \tag{1}$$

Where, C_H represents the total mass of the charge in the hexagonal prism formed by combination and allocation; C_i' represents the mass of the charge after the reduction of C_i participating in the combination allocation process, $i = 1,2,3$; m_1 is the common mass of three groups of sandwich charge after combination and allocation; m_2 is the mass shared by the adjacent two groups of sandwich charges after combination and allocation; m_3 is the mass of each of three groups of sandwich charges after combination and allocation.

In order to further determine the charge mass C_i' of the reduced sandwich charge in Eq. (1), we analyze it from the perspective of combination and allocation. It can be seen from Figure 1 (c) that there are three charge areas in the hexagonal prism charge warhead formed by the combination: magenta area, yellow area, and cyan area. The magenta

area is the charge formed by the superimposition of sandwich charges No. 1, 2, and 3. Therefore, this part of the charge is shared by three groups of sandwich charges, that is, each group of sandwich charges in the superimposed hexagonal prism accounts for 1/3 of the mass of the magenta part. The yellow area is formed by the superimposition of sandwich charges No. 1 and 2, No. 2 and 3, and No. 1 and 3. Therefore, this part of the charge is shared by two adjacent groups of sandwich charges; that is, each group of sandwich charges in the superimposed hexagonal prism accounts for 1/2 of the mass of the yellow part. The cyan area is the charge of the three sandwich charges, No. 1, 2, and 3, that did not participate in the combination. Therefore, this cyan part of the charge is shared by each of the three groups of sandwich charges separately. According to the combination, allocation, and Eq. (1), C_i' can be calculated by the following Eq. (2):

$$C_i' = \frac{1}{3}m_1 + 2m_2 + \frac{4}{2}m_3 = \frac{1}{3}C_H = \frac{2}{6}C_H \tag{2}$$

In conclusion, we refer to the phenomenon of the combination and allocation of sandwich charges to form prismatic charges as the superposition effect of prismatic charges.

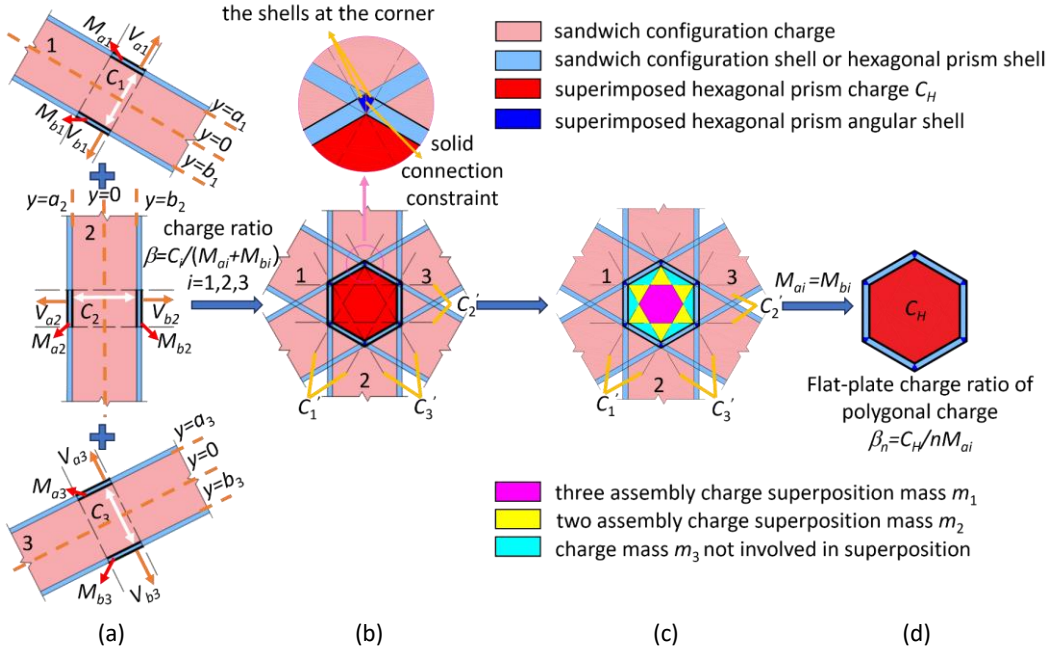

Figure 1. Configuration decomposition analysis of the hexagonal prism charge warhead.

2.2 Model establishment

To derive a fragment velocity model of the hexagonal prism charge warhead, we mainly start from energy conservation and configuration decomposition. For the hexagonal prism charge warhead formed by combination and allocation, based on Eq. (1), we can obtain the following energy conservation equation:

$$C_H E = C_1'E + C_2'E + C_3'E \tag{3}$$

Where E is the energy released per unit mass of explosive, which is the Gurney energy.

To determine the total energy ($C_i'E$) of a single sandwich charge after combination and allocation in Eq. (3), an energy conservation analysis was performed on a single sandwich charge below. In the hexagonal prism charge warhead formed by combination and allocation, as shown in Figure 1, the chemical energy of each of the three sandwich charges after combination and allocation equals the sum of the kinetic energies of their respective shells and detonation products between shells. From the perspective of combination, in addition to the rectangular shells of each independent plate, there are also shells at the corners, which obtain the corresponding kinetic energy. After the combination, solid connection constraints are formed between adjacent shells, and the failure of the constraints also generates energy

consumption. We denote the energy consumed by angular shells and the constraint failure of the single sandwich charge after combination and allocation as an energy consumption function *G*. Since the angular shells and the constraint failure energy consumption are both in the form of energy, to consider it and facilitate subsequent theoretical deduction, we use the kinetic energy of a single plate M_{ai} as the energy unit, and its *k* times can be used to express it as the angular shells and the constraint failure energy consumption. Then we can make assumptions such as: the function *G* is *k* times the kinetic energy of the plate M_{ai} (i.e., $G = k*(M_{ai}V_{ai}^{\ 2}/2)$), where *k* is an unknown term. Therefore, for a single sandwich charge after combination and allocation, its energy conservation equation can be written as:

$$C_i'E = \frac{1}{2}(M_{ai}V_{ai}^{\ 2} + M_{bi}V_{bi}^{\ 2}) + \frac{1}{2}\int_0^{a_i} V^2(y_i)\rho(y_i)dy_i + \frac{1}{2}\int_0^{b_i} V^2(y_i')\rho(y_i')dy_i' + k*\frac{1}{2}M_{ai}V_{ai}^{\ 2} \tag{4}$$

Where M_{ai} and M_{bi} are the mass of the rectangular shells on both sides of the sandwich charge, respectively; V_{ai} and . V_{bi} . are the velocities of the mass M_{ai} and M_{bi} plate, respectively; *y* represents the distance of the product gas from the zero-velocity plane; y_i' denotes the opposite direction of y_i ; a_i and b_i are the distance from the shell M_{ai} and M_{bi} to the zero-velocity plane, respectively; k is an unknown function.

Applying the assumption of uniform expansion of the product gas in the sandwich charge (in an explosive metal system, after the explosive detonation, it is assumed that the product gas expands uniformly and that the density is equal everywhere). Of course, the assumption of uniform gas density of the product is not true, because the gas density near the explosive reaction zone is obviously higher. The uniform density assumption will cause the velocity to be low. However, neglecting rarefaction wave effects leads to overestimated velocities. Therefore, this assumption is accurate within a fairly wide range of charge ratio β (0.1~5.0, β is defined as the ratio of the charge mass to the metal mass of the charged warhead.) (Wang 2019), the relationship of $\rho(y_i)$ in the single sandwich charge after combination and allocation is as follows:

$$\rho(y_i) = \rho(y_i') = \frac{C_i'}{a_i + b_i} \tag{5}$$

Based on the assumption of linear velocity, the calculation model for velocity at points y_i and y_i' is (In an explosive metal system, after the explosive detonation, the detonation gas will form a stable plane at a certain position in the plates on both sides. The product gas velocity is 0 at the plane position. For the sake of computational simplicity, it is assumed that the velocity of the product gas changes linearly in the radial direction from the stable plane to the two side shells, and remains equal to the velocity of the shell's movement during its passage through the shell thickness.) (Wang 2019):

$$V(y_i) = \frac{y_i}{a_i}V_{ai} \tag{6}$$

$$V(y_i') = \frac{y_i'}{b_i}V_{bi} \tag{7}$$

Substituting Eq. (5) into Eq. (7) into Eq. (4), we obtain

$$C_i'E = \frac{V_{ai}^{\ 2}}{2}\left[M_{ai} + M_{bi}(\frac{b_i}{a_i})^2 + \frac{a}{3}\times\frac{C_i'}{a_i + b_i} + (\frac{b_i}{a_i})^2\times\frac{b_i}{3}\times\frac{C_i'}{a_i + b_i} + kM_{ai}\right] \tag{8}$$

Since the hexagonal prism shell is a regular hexagonal prism and detonates at a central point, there are $M_{ai} = M_{bi}$ and $a_i = b_i$. Then, substituting Eq. (2) and (8) into Eq. (3), we can obtain:

$$V_{ai}=\sqrt{\frac{2}{6}}\sqrt{2E}\left[\frac{(2+k)M_{ai}}{C_H}+\frac{C_i'}{3C_H}\right]^{-1/2}=\sqrt{\frac{2}{6}}\sqrt{2E}\sqrt{\frac{3C_H}{3(2+k)M_{ai}+C_i'}} \tag{9}$$

Letting $\beta_n=\frac{C_H}{nM_{ai}}$, which denotes the flat-plate charge ratio of the polygonal charge, and n represents the number of sides of the polygonal charge. For a hexagonal prism, n=6, then Eq. (9) can be simplified as:

$$V_{ai}=\sqrt{2E}\sqrt{\frac{\beta_n}{(1+k/2)+\beta_n/3}} \tag{10}$$

To determine the unknown function *k* in Eq. (10), we further analyze the combination in Figure 1. There are two extreme cases of the combination: 1. When *n*=2, that is, there is no angular shells, constraints and combination (as shown in Figure 1 (a)), then Eq. (10) is Gurney equation for calculating sandwich charges:

$$V_0=\sqrt{2E}\sqrt{\frac{\beta_n}{1+\beta_n/3}} \tag{11}$$

2. When *n*=+∞, that is, the polygon is a cylinder, then Eq. (10) is the Gurney equation for calculating cylindrical charges:

$$V_0=\sqrt{2E}\sqrt{\frac{\beta_n}{1+\beta_n/2}} \tag{12}$$

Through the analysis of the two limit boundary conditions, it can be known that when *n*=2, $k=0$ in Eq. (10); When *n*=+∞, $k/2=\beta_n/6$ in Eq. (10). Based on this, we have constructed the following function k to satisfy the above two boundary conditions:

$$k=2*[(\beta_n/6)^{\frac{n-2}{n-m}}+\frac{n-2}{n-m}-1] \tag{13}$$

Where *n* is the number of sides of the polygon, m is a constant.

For a given hexagonal prism, only *m* is an unknown term in Eq. (13).

By substituting Eq. (13) into Eq. (10), we obtain the model for calculating the fragment maximum velocity V_M of a hexagonal prism charge warhead based on energy conservation from the perspective of configuration decomposition:

$$V_M=V_{ai}=\sqrt{2E}\sqrt{\frac{\beta_n}{\left[(\beta_n/6)^{\frac{n-2}{n-m}}+\frac{n-2}{n-m}\right]+\beta_n/3}} \tag{14}$$

Eq. (14) calculates the fragment maximum velocity of hexagonal prism charge warheads without considering rarefaction waves. In practical engineering, achieving the large aspect ratio needed to suppress rarefaction wave effects can be challenging for hexagonal prism charge warheads. As a result, their fragment velocities are susceptible to end rarefaction wave effects to varying degrees. To accurately determine the fragment velocity and evaluate the damage efficiency of such warheads, it is crucial to establish a theoretical model that considers the influence of axial rarefaction waves on fragment velocity.

Based on Eq. (14), we introduce a correction term F to account for the influence of rarefaction waves on the axial fragment velocity. The specific form of the correction function *F* requires further study on the correlation between the

aspect ratio and the fragment velocity. Therefore, the calculation model considering the influence of rarefaction waves' effect on the fragment velocity of the hexagonal prism charge warhead is as follows:

$$V_M = V_{ai} = F * \sqrt{2E} \sqrt{\frac{\beta_n}{\left[(\beta_n / 6)^{\frac{n-2}{n-m}} + \frac{n-2}{n-m}\right] + \beta_n / 3}} \tag{15}$$

3 NUMERICAL SIMULATION

To accurately determine the constant m and the rarefaction wave influence function *F* in Eq. (15), it is necessary to study the influence laws of the aspect ratio and charge ratio on the fragment velocity. Based on the obtained influence law, the influence law of the charge ratio on the fragment velocity of the charge, we can determine the unknown constant m in Eq. (15). Based on the obtained influence law of the aspect ratio on the fragment velocity of the charge, we can determine the unknown function *F* in Eq. (15). Finally, the complete calculation model for the fragment velocity was given. The numerical simulation method was used to carry out the influence laws of the aspect ratio and charge ratio on the fragment maximum velocity of the charge (Cullis et al. 2014; Grisaro and Dancygier 2015).

3.1 Numerical model

A numerical model of the hexagonal prism charge warhead, as illustrated in Figure 2, was established based on the size of the test warhead specimens. The hexagonal prism charge warhead lacked end caps. Given the symmetry of the hexagonal prism, a quarter model was developed using CATIA, meshed in HyperMesh, and subsequently converted into an SPH model in Autodyn, as shown in Figure 2. In Figure 2, *D* is the diameter of the circumcircle of the hexagonal charge, *L* is the length of the charge and the shell, and *h* is the thickness of the shell. The aspect ratio of the charge is defined as the ratio of the charge length *L* to the circumscribed circle diameter *D* of the charge (in Figure 2). The detonation mode was set to single-point detonation due to the use of a detonator, with the detonation point positioned identically to that of the detonator in the test warhead specimen. To accurately determine the fragment velocity, SPH particle size was generally set to no more than 0.4 mm (An et al. 2018; Guo et al. 2020; Huang et al. 2023; Li et al. 2023c). Through particle size independence analysis, an SPH particle size of 0.3 mm was selected for the simulation. At the 60° position, Gauge points were arranged along the axial direction of the SPH model and placed on the outer side of the shell, as depicted in Figure 2.

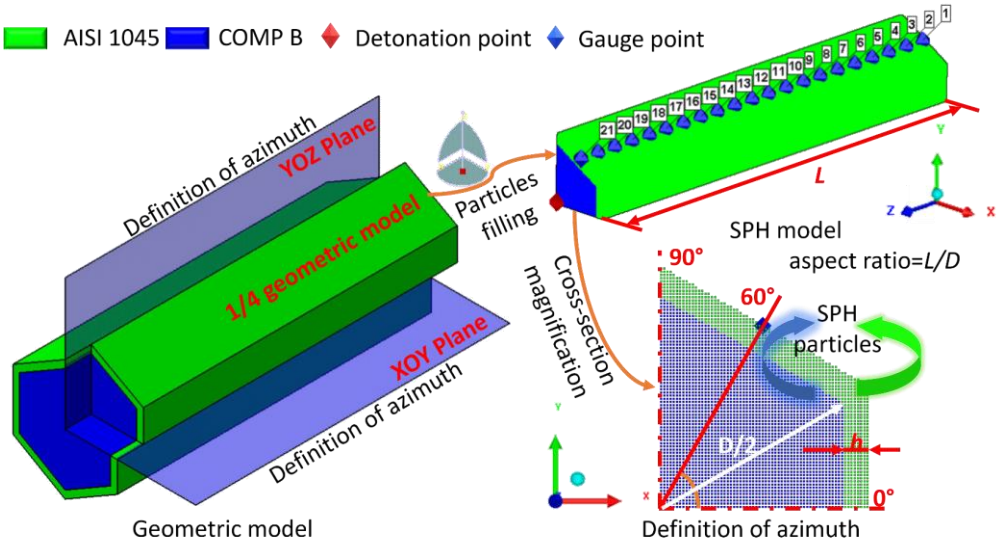

Figure 2. Numerical model and Gauge points layout.

3.2 Material constitutive

The hexagonal prism charge warhead model was composed of AISI1045 steel and Comp-B explosive. AISI1045 steel adopted the Johnson-Cook constitutive model (Johnson 1983):

$$\sigma = (A + B\bar{\varepsilon}^{n})(1 + C\ln\varepsilon_r^{*})(1 - T^{*m}) \tag{16}$$

Where $\bar{\varepsilon}$ is the equivalent plastic strain; ε_r^{*} is the relative equivalent plastic strain rate; $T^{*} = (T - T_0)/(T_m - T_0)$ is the relative temperature, T_0 is the reference temperature and the room temperature is generally taken; T_m is the melting point of the material; T is the instantaneous temperature; A is yield stress; B is the strain hardening coefficient; n is the strain hardening index; C is the strain rate correlation factor; m is the temperature correlation factor.

The principal strain failure was selected as the failure criterion for the steel shells, and the Mott random failure model was used to simulate the fragments accurately. The random failure model is expressed as (Mott 1947):

$$dp = (1 - p)Ce^{\gamma\varepsilon}d\varepsilon \tag{17}$$

Where $(1-P)$ is the probability of strain non-fracture less than ε , C and γ are material constants. According to Mott's theory, γ can be estimated by the following equation:

$$\gamma \approx 160\frac{\sigma_2}{\sigma_f(1 + \varepsilon_f)} \tag{18}$$

Where σ_f and ε_f are the true stress and true strain of the failure point, and σ_2 is the strength enhancement coefficient.

The Hopkinson bar dynamic tensile test of AISI1045 steel was carried out. Figure 3 shows the installation arrangement and results after breaking the dynamic tensile specimens. The JC model parameters obtained from the test are detailed in Table 1, and the average principal tensile failure strain is 0.23. The curves and experimental data fitted based on the data of Table 1 are shown in Figure 4. By comparing the fitting results with the experimental results, it can be found that the fitting results and the experimental results have a good overlap, and it is believed that the fitting results of this constitutive model have high reliability.

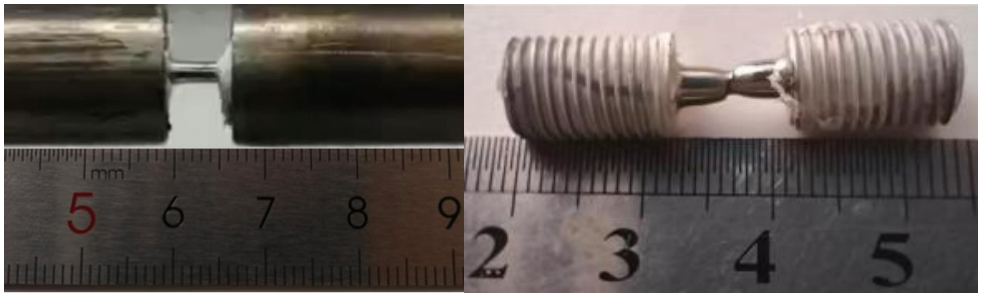

Figure 3. AISI1045 steel Hopkinson bar dynamic tensile test.

Table 1. Parameters of steel Johnson-Cook.

ρ (g/cm^3)	A (MPa)	B (MPa)	n	C	m	T_m (K)	γ
7850	497	314	0.25	0.06	1.03	1793	54.0

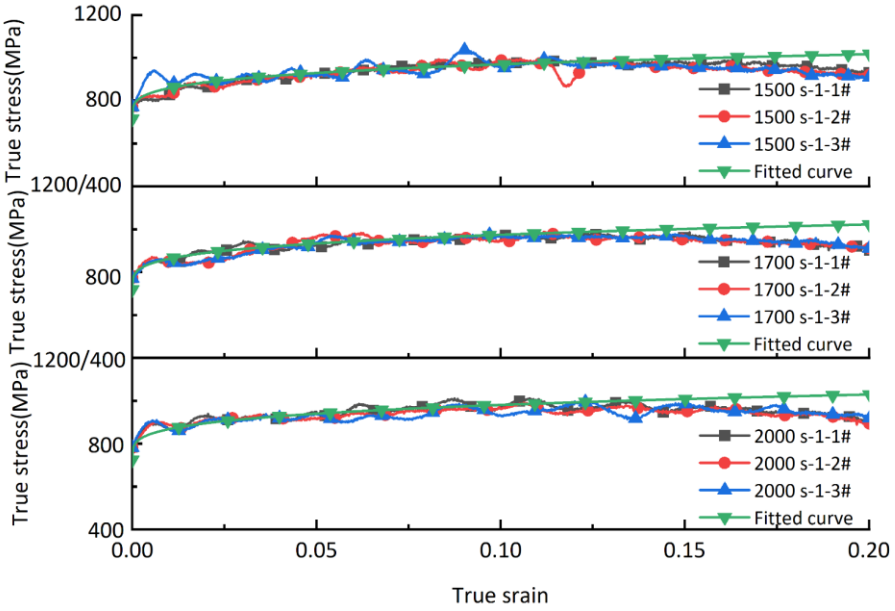

Figure 4. Comparison of fitted curves and experimental results under different strain rates.

The JC model needs to be combined with the shock equation of state, which is widely used and can fully represent most materials. The equation of state adopts the basic relationship between the particle velocity and the shock wave velocity $U = c_0 + su_p$, and its form is as follows:

$$P = P_H + \Gamma\rho(e - e_H) \tag{19}$$

Where it is assumed that $\Gamma\rho = \Gamma_0\rho_0$ is a constant, Γ_0 is the Gruneisen coefficient, ρ and ρ_0 are the current density and the initial density, respectively. P_H and e_H are the pressure and internal energy of the point on the Hugoniot curve, respectively. P_H and e_H are given by the following equation:

$$P_H = \frac{\rho_0 c_0 u(1+u)}{[1-(s-1)u]^2} \tag{20}$$

$$P_H = \frac{P_H}{2\rho_0}\left(\frac{u}{1+u}\right) \tag{21}$$

Where $u = \rho/\rho_0 - 1$, c_0 is the volume sound velocity, and s is the material parameter to be determined by the test. For steel, Γ_0 is 2.17, and the values of c_0 and s are 4569 m/s and 1.49 m/s, respectively (Kong et al. 2013).

Comp-B explosive is described by the JWL equation of state (Jones-Wilkins-Lee EOS):

$$P = A\left(1 - \frac{\omega}{R_1 V}\right)e^{-R_1 V} + B\left(1 - \frac{\omega}{R_2 V}\right)e^{-R_2 V} + \frac{\omega E_0}{V} \tag{22}$$

Where P is the detonation pressure; $V = v/v_0$ is the relative volume; v is the volume of the detonation product; v_0 is the initial volume of the explosive; E_0 is the initial internal energy density; A, B, R_1, R_2, and ω are the parameters related to the properties of explosives obtained by experiments.

Because the Comp-B explosive is a very mature explosive, and the die-casting technology is also very mature, the parameters of the JWL equation of state are basically unchanged when the density of the explosive is constant. The average density of the Comp-B explosive used in this paper was 1.671 g/cm^3, which was only 2.71% different from the

density of the Comp-B explosive in the Autodyn material library. Therefore, this paper adopted the model parameters of Comp-B explosives from the Autodyn material database, as shown in Table 2 (C D 2011; Wang 2019).

Table 2. JWL parameters of the explosive model.

ρ (g/cm^3)	D (m/s)	P_{CJ} (GPa)	E_0 (KJ/m^3)	C_1 (GPa)	C_2 (GPa)	R_1	R_2	ω
1.717	7980	29.5	8.5×10^6	524.23	7.678	4.2	1.1	0.34

3.3 Influence factors analysis

Utilizing the SPH model of a hexagonal prism charge warhead as illustrated in Figure 2 of Section 3.1, configured with a shell thickness of 2.6 mm, a charge circumcircle diameter of 40 mm, an axial length of the charge and shell of 120 mm, and an SPH particle diameter of 0.3 mm, a systematic investigation was conducted to ascertain the influence law of the aspect ratio and charge ratio on fragment velocities. The aspect ratio was varied by manipulating the axial length of the charge and shell, thereby facilitating an analysis of its impact on fragment velocities. Furthermore, the charge ratio was altered by adjusting the shell thickness, enabling a comprehensive study of the effects of different charge ratios on fragment velocities.

3.3.1 Effect of aspect ratio

Previous studies have demonstrated that axial rarefaction waves exert a significant influence on the fragment velocity of warhead shells (Gao et al. 2019; Liu et al. 2022). For warheads without end caps, when the aspect ratio is 3.0, the impact of end rarefaction waves on the fragment maximum velocity is essentially nullified under end-center initiation. When the aspect ratio is 4.0, the influence of end rarefaction waves on the fragment maximum velocity can be almost completely mitigated (Liu et al. 2022; Li et al. 2023b). Utilizing a numerical simulation method, simulations of hexagonal prism charge warheads with varying aspect ratios were conducted to elucidate the variation law of fragment velocities under the influence of axial rarefaction waves. This research is essential for advancing the establishment of a calculation equation for fragment velocities in hexagonal prism charge warheads.

Hexagonal prism charge warheads with aspect ratios ranging from 0.3 to 4.0 were simulated by adjusting the charge and shell lengths, with all other model parameters held constant. The arrangement of Gauge points corresponds to Figure 2. The detonation was initiated at the end center, and numerical simulation research was conducted on the detonation-driven fragment process and variation in fragment velocities. Figure 5 illustrates fragments' dispersion from hexagonal prism charge warheads with varying aspect ratios. It is observed that as the aspect ratio increases, the expansion pattern of fragments along the axial direction transitions from parabolic to trapezoidal. When the aspect ratio exceeds 2.5, the fragments of the hexagonal prism display an approximate planar area in the axial direction, suggesting minimal influence from rarefaction waves. Figure 6 presents the axial velocity distribution of fragments from hexagonal prism charge warheads with different aspect ratios. The axial velocity of fragments is observed to increase with the aspect ratio, exhibiting a rapid initial rise followed by a slower progression, approaching stabilization around an aspect ratio of 4.0.

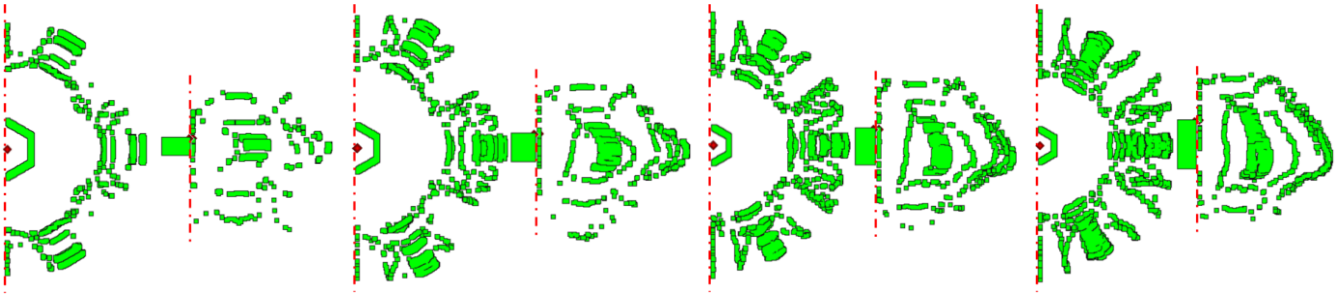

(a) Aspect ratio 0.3 (b) Aspect ratio 0.6 (c) Aspect ratio 1.0 (d) Aspect ratio 1.5

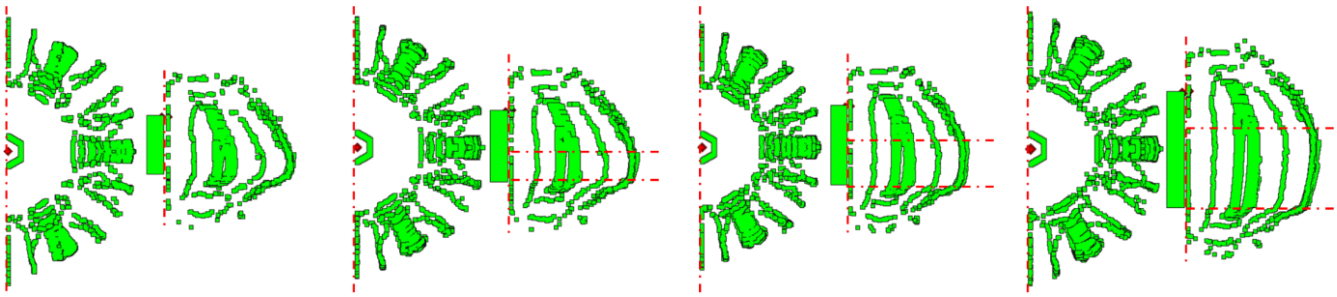

(e) Aspect ratio 2.0 (f) Aspect ratio 2.5 (g) Aspect ratio 3.0 (h) Aspect ratio 4.0

Figure 5. Fragment dispersions with different aspect ratios.

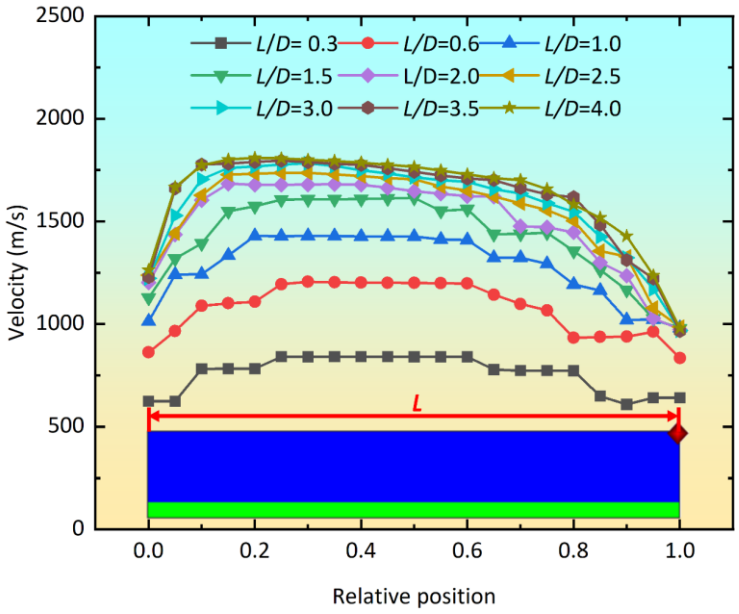

Figure 6. Velocity distributions with different aspect ratios.

The fragment velocity increases first and then decreases along the axial direction, mainly because the fragment velocity at both ends of the charge decreases due to the rarefaction waves at the near and far ends of the charge. However, far from the detonation end, the fragment reaches the maximum velocity, and the position where the maximum velocity appears is 0.15L~0.3L. With the increase of aspect ratio, the area in span that is not affected by end rarefaction waves becomes larger and larger. Moreover, when the aspect ratio $L/D \geq 3.0$, the fragment axial velocity is almost no longer affected by rarefaction waves, which well explains the fragment platform segment in Figure 5 (g) and (h). The true fragment maximum velocity can be obtained by increasing the aspect ratio. Consequently, the maximum velocity of the fragments from the simulation results was calculated as a parameter for subsequent research.

3.3.2 Effect of charge ratio

In addition to the aspect ratio of the charge, the charge ratio is also a significant factor influencing the fragment velocity. Figure 5 and Figure 6 illustrate that, for an aspect ratio of 4.0, the axial velocity of the hexagonal prism charge warhead is nearly unaffected by the axial rarefaction wave. To further verify and analyze the above-mentioned action law of the rarefaction wave, Figure 7 presents the figures of detonation wave propagation and rarefaction wave action processes with aspect ratios of 0.6 and 4.0, respectively. As shown in the figures, with the increase of charge length, the detonation wave generated at the initiation end gradually transforms from a spherical wave to a plane wave when propagating axially to the opposite end. At both ends of the charge, the rarefaction waves reflected at the charge interface and casing interface catch up with and unload the forward-propagating detonation wave. This decreased the detonation wave pressure and affected the driving velocity of fragments at the two ends. Thus, this led to the distribution trend that fragments at both ends of the charge are small-sized, and their velocity reduces, as presented in Figure 5 and Figure 6. In contrast, a zone with stable driving velocity is formed in the middle section of the charge where plane waves

generate and propagate. This result is highly consistent with the axial dispersion profile of fragments in Figure 5 and the plateau section of fragment velocity in the middle part of the charge in Figure 6. The above analytical results fully verify the action of rarefaction waves and their influence law on fragment velocity.

In summary, the aspect ratio of 4.0 can be adopted as the charge aspect ratio for subsequent studies on other influencing factors. Therefore, to investigate the influence of the charge ratio on the fragment velocity of the hexagonal prism charge warhead, simulations were conducted based on the SPH model of the hexagonal prism charge warhead with an aspect ratio of 4.0. By varying the shell thickness to 2 mm, 2.6 mm, 3 mm, 4 mm, 5 mm, and 6 mm, hexagonal prism charge warheads with different charge ratios were simulated and analyzed, with all other model parameters held constant. The distribution pattern of the axial velocity of the hexagonal prism charge warhead concerning the charge ratios was obtained, as depicted in Figure 8. As shown in the figure, with the increase of casing thickness, the charge ratio β_n of the charged warhead decreases, and the fragment velocity reduces gradually, with the declining trend tapering off progressively. This is mainly because when the charge remains unchanged, adjusting the casing thickness increases the mass of fragments. Thus, under the condition that the total driving energy stays constant, the fragment velocity decreases accordingly.

Furthermore, under the same aspect ratio, the axial velocity distribution trend of the fragments under different charge ratios is consistent. The results also indicate that the axial fragment velocity gradually decreases with increasing shell thickness, and the fragment maximum velocity appears at the position of 0.25*L*. The maximum fragment velocity appears at 0.25*L* instead of the mid-span of the charged warhead, which is mainly related to the propagation of the plane detonation wave. During propagation, it is barely subjected to unloading by rarefaction waves catching up from the rear. Thus, with continuous detonation of the charge, the velocity of casing fragments along the detonation wave propagation direction increases gradually.

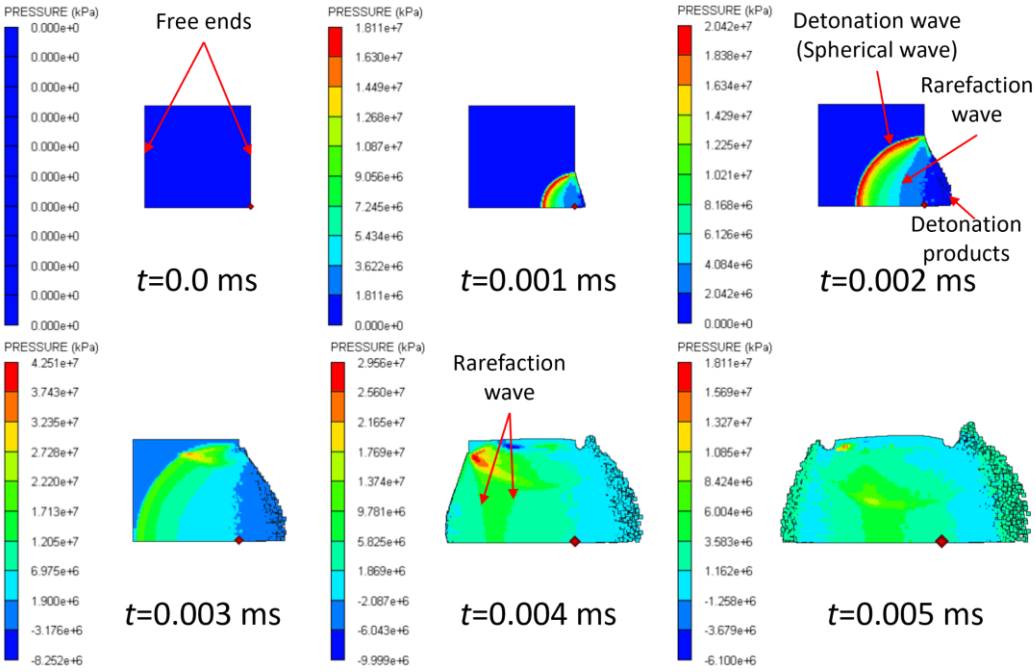

(a) *L*/*D*=0.6

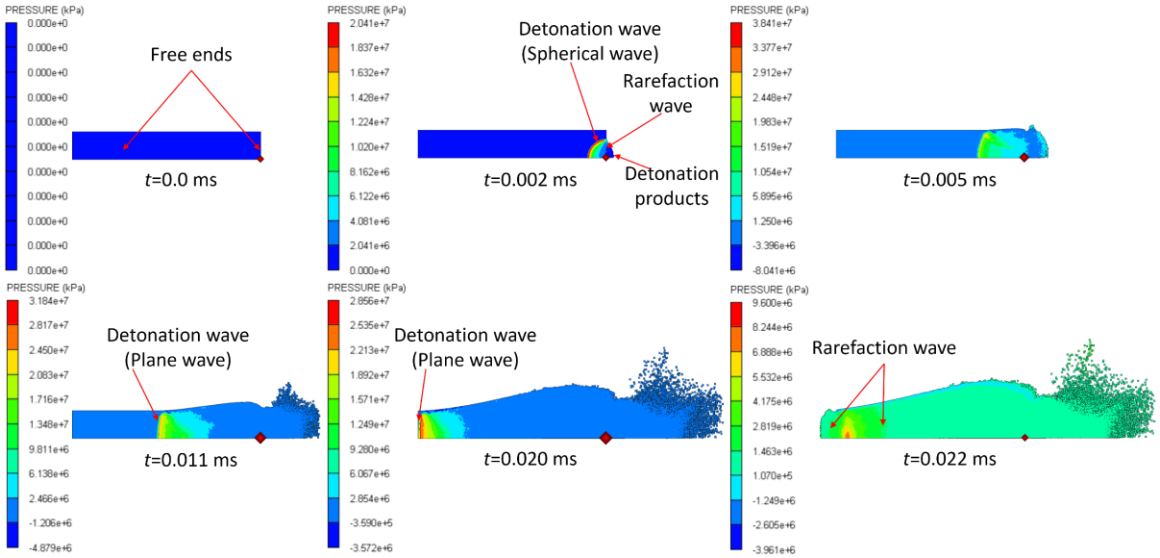

(a) *L/D*=4.0

Figure 7. Propagation process of detonation wave along the axial direction.

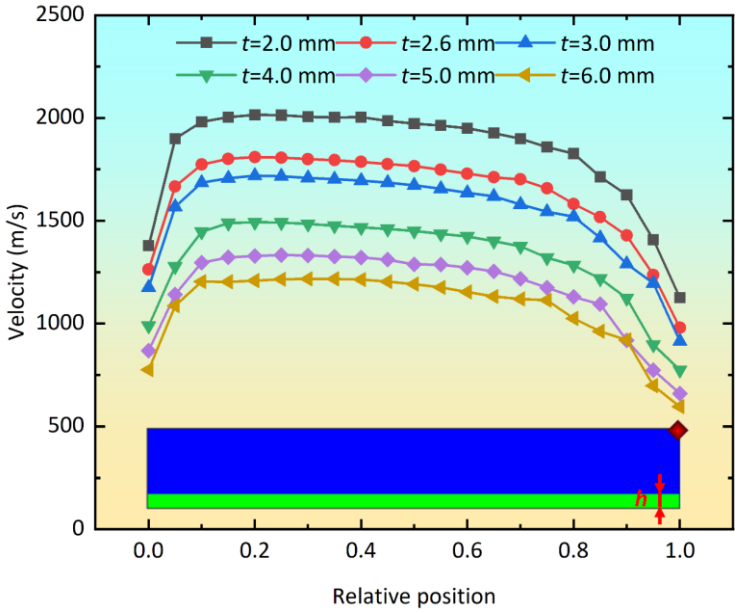

Figure 8. Velocity distribution of different shell thicknesses.

3.4 Model parameter determination

Section 3.3.2 calculates the axial fragment velocity distribution of the hexagonal prism charge warhead model under different charge ratios, almost unaffected by axial rarefaction waves. Section 2.2 obtained a new calculation, Eq. (14) of the fragment maximum velocity of the prism charge warhead, without considering the influence of axial rarefaction waves through theoretical derivation. To determine the unknown parameters m of Eq. (14), we fitted the simulation data of the fragment maximum velocity of the large aspect ratio hexagonal prism charge warhead obtained in Section 3.3.2 for shells of different thicknesses. The fitting results are shown in Figure 9 $R^2 = 99.264\%$. Thus, we obtained the calculation model used to calculate the maximum velocity of the fragments:

$$V_M = \sqrt{2E}\sqrt{\frac{\beta_n}{\left[(\beta_n/6)^{1.41827}+1.41827\right]+\beta_n/3}} \tag{23}$$

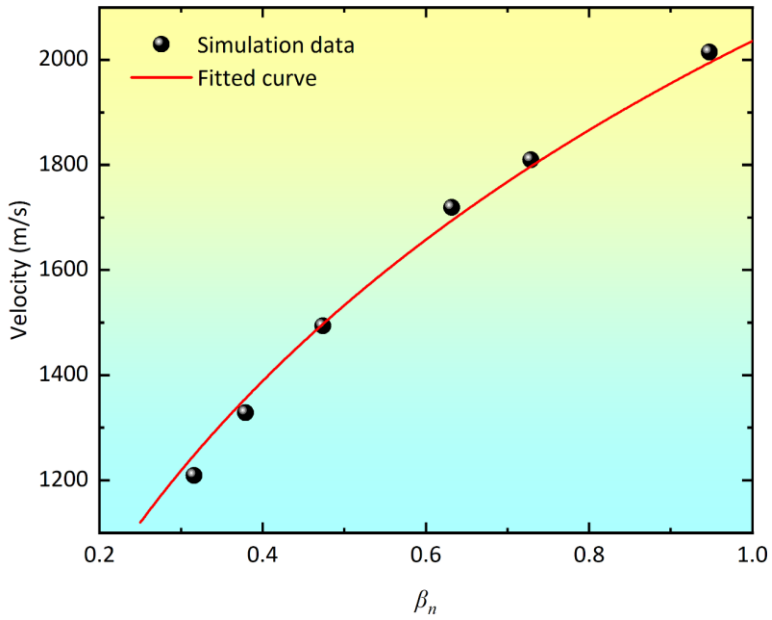

Figure 9. Comparison of the established model with simulation results.

To accurately calculate the axial fragment velocity based on Eq. (23), we introduce a correction term F to account for the influence of rarefaction waves on the axial fragment velocity in Section 2.2. This correction term F is solely a function of the aspect ratio. Section 3.3.1 simulates hexagonal prism charge warheads with aspect ratios of 0.3, 0.6, 1.0, 1.5, 2.1, 3.0, 3.5, and 4.0. Figure 9 illustrates how the axial fragment velocity distribution varies with different aspect ratios. We can discover the following rules: 1. When the aspect ratio is zero, implying an absence of the charge, the fragment velocity is zero. 2. Figure 9 shows that the axial fragment velocity increases with the aspect ratio but at a decreasing rate. Hence, the function F must satisfy certain conditions:

(1) The correction F must pass through the (0,0) point.

(2) It is an increasing function of the aspect ratio;

(3) The fragment maximum velocity decreases with the increase of the aspect ratio.

Based on the above conditions, it is assumed that the function expression of the correction term F is:

$$F = \mathrm{k}_1 * \left(1 - \frac{1}{1+(\mathrm{k}_2 * L/D)^{\mathrm{k}_3}}\right) \tag{24}$$

Where k_1, k_2, and k_3 are the fitting coefficients; L/D is the aspect ratio of the hexagonal prism charge warhead.

The axial velocity of the hexagonal prism charge warhead was calculated at different aspect ratios, as presented in Section 3.3.1. Therefore, the undetermined parameters k_1, k_2, and k_3 of the correction function F can be obtained by fitting the maximum velocity data presented in Section 3.3.1. The fitting results are shown in Figure 10 $\mathrm{R}^2 = 99.972\%$. Therefore, we consider the influence of the aspect ratio on the fragment velocity of the hexagonal prism charge warhead, and the model for calculating the fragment velocity of hexagonal prism charge warheads is as follows:

$$V_{\mathrm{M}} = 1.09378 * \left(1 - \frac{1}{1+(2.52496 * L/D)^{1.08784}}\right) * \sqrt{2E}\sqrt{\frac{\beta_n}{\left[(\beta_n/6)^{1.41827} + 1.41827\right] + \beta_n/3}} \tag{25}$$

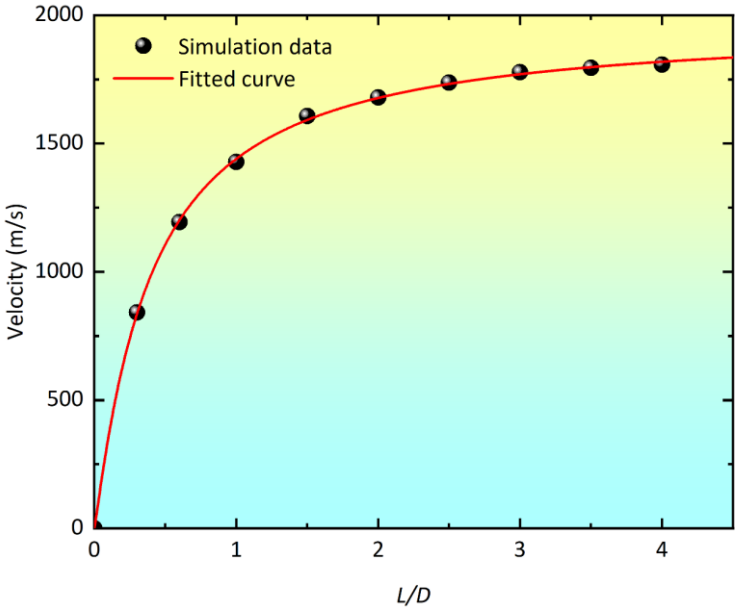

Figure 10. Data fitting of maximum velocities under different aspect ratios.

4 EXPERIMENT

4.1 Specimen design

Research has demonstrated that the axial rarefaction wave effect notably influences fragment velocity. To mitigate this effect in practical applications, strategies such as enhancing the aspect ratio and appending end caps have been employed (Guo et al. 2019a; Liao et al. 2021; Li et al. 2023b; Gao et al. 2023). Taking into account the safety and the accuracy of fragment velocity measurement, we conducted the experimental research using an L/D=3.0 charge warhead. In this study, X-ray photography technology, which can clearly capture the outline of fragment scattering, was used to carry out experiments (Ramudu et al. 2019; Li et al. 2024b). Given the substantial challenges end cap additions pose for X-ray equipment protection, this investigation focuses on aspect ratio augmentation as a suppression measure. Figure 11 illustrates the design of the hexagonal prism charge warhead, characterized by a circumcircle diameter D of its main charge, shell thickness h , an internal Comp-B explosive charge, and an AISI1045 steel shell. Ignition is achieved via single-point detonation at the center of the end face, facilitated by a hollow cork securing the detonator centrally on one warhead extremity. Experimental specimens, depicted in Figure 12, were fabricated for the study, with detailed specifications summarized in Table 3.

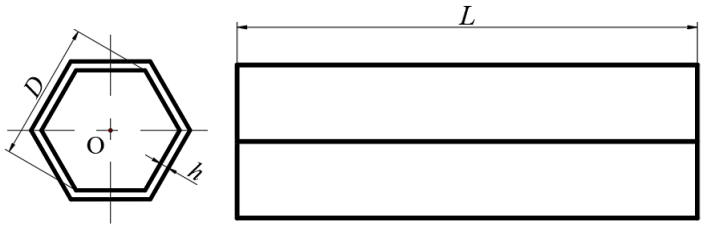

(a) Front view (b) Side view

Figure 11. Hexagonal prism charge warhead structure diagram.

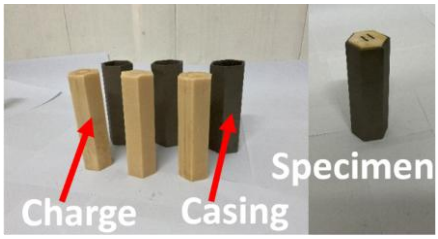

Figure 12. Hexagonal prism charge warhead specimens.

Table 3. Test specimen parameters.

No.	L (mm)	D (mm)	h (mm)	Charge weight(g)	ρ (g/cm³)	L/D
1#	122.2	40	2.6	208.7	1.676	3.03
2#	124.67	40	2.6	211.9	1.665	3.02

4.2 Experimental setup

The hexagonal prism charge warhead's static explosion test is depicted in Figure 13, which illustrates both the schematic and the actual arrangement. Utilizing two parallel Scandiflash CVR 450 X-ray tubes, we captured dispersion images of the detonation-driven fragments at distinct intervals. Figure 13 (a) outlines the X-ray shooting principle schematically. The X-ray capture times are detailed in Table 4. Before detonation, each X-ray tube secured a static image; after detonation, they sequentially captured dynamic images at two distinct moments onto the film. Figure 13 (b) presents the schematic of velocity targets adjacent to the test specimen. This target verified the precision of the X-ray test velocity measurements, corroborating the outcomes. Table 4 also lists the velocity targets' positioning distance. Beneath the test warhead specimen, two reference balls were horizontally aligned, as indicated in Figure 13 (b). These served dual purposes: determining the image magnification ratio by comparing actual and captured sizes, and aligning the X-ray image contours at various times to streamline subsequent processing. The actual experimental setup is displayed in Figure 13 (c), with the test warhead specimen sandwiched between the X-ray tube and the film, supported by a wooden frame and a paper cup. The detonating detonator was positioned on the side nearest the X-ray tube to minimize potential equipment damage.

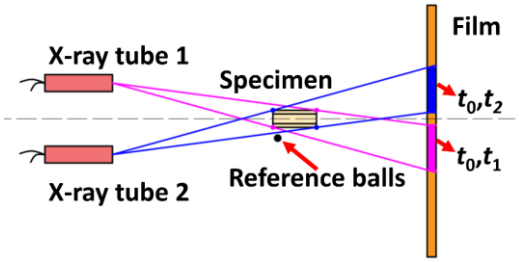

(a) Schematic of the test setup

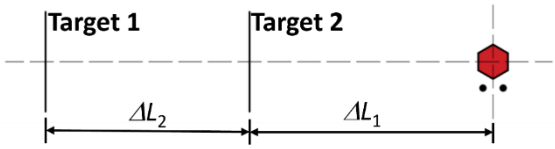

(b) Schematic of the velocity target

(c) Actual test setup

Figure 13. Test setup and schematic.

Table 4. X-ray test parameters.

No.	t_0 (μs)	t_1 (μs)	t_2 (μs)	ΔL_1 (cm)	ΔL_2 (cm)
1#	0	25.641	40.581	132	102
2#	0	25.575	40.556	132	107.5

4.3 Proceeding methods

Figure 14 (a) illustrates the typical dynamic images of a hexagonal prism charge warhead shell captured by X-ray tubes at times t_0, t_1, and t_2. Due to the vertical arrangement of the X-ray tubes, the resultant images are displayed accordingly. By analyzing the fragment images at times t_1 and t_2, we can calculate the velocities of fragments in various azimuths. However, this experiment employed a hexagonal prism charge warhead with an aspect ratio of 3.0, a relatively

large ratio that causes the end debris to shield the X-ray imaging process. As depicted in Figure 13 (a), rays from the two X-ray tubes were obstructed by the charge's ends. This shielding effect increases the velocity error for fragments at different azimuth angles when measured via X-ray images, potentially leading to inaccurate velocity measurements (Ramudu et al. 2019). Consequently, the circumferential velocity distribution of fragments from a large aspect ratio charge warhead cannot be reliably determined through X-ray image analysis. Nonetheless, due to the vertical configuration of the X-ray tubes, this shielding does not affect the measurement of maximum velocities in the left and right directions. Therefore, maximum velocities on the left and right sides were ascertainable. Subsequent processing of X-ray images of hexagonal prism charge warheads enabled the calculation of maximum velocities on both the left and right horizontal sides of shells.

The captured X-ray images underwent processing. Initially, the magnification ratio of the X-ray images was determined by comparing the actual size of the reference balls to their size on the X-ray images. The magnification ratio, d, was defined as the ratio between the image size in the dynamic image and the actual size. AUTOCAD software was employed to measure the image size of the reference balls in the dynamic images, and it was also used to obtain the outlines of the shells at different times. Based on the relative positions of the balls, the different outlines were converted into the same coordinate system by using the 'Align' function in AUTOCAD (Li et al. 2023a), as illustrated in Figure 14. Subsequently, two radial lines were drawn from the center of the static outline, each intersecting with two dynamic outlines. The distance between the two intersections was measured, and this distance was divided by the magnification ratio and the image capture time interval to obtain the fragment velocities at 0° and 180° azimuth angles:

$$V_j = \frac{\Delta x}{t_2 - t_1} * \frac{1}{d} (j = 0, 180) \tag{26}$$

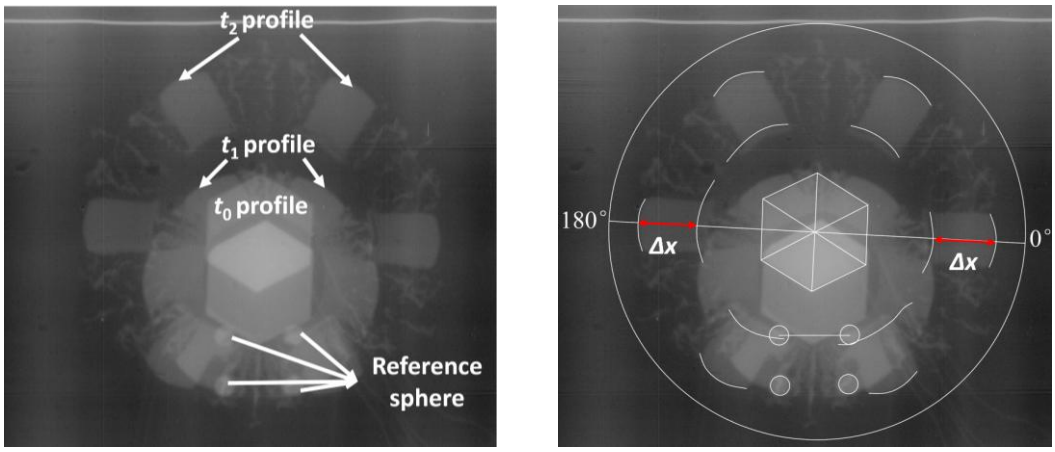

(a) Dynamic image (b) Processed result

Figure 14. Data processing method.

4.4 Experimental results

According to the processing method of test results in Section 4.3, the fragment velocity V_t obtained from the velocity target, X-ray image magnification ratio, and fragment velocities V_0 and V_{180} at 0° and 180° azimuth angles for 1# and 2# charges are presented in Table 5. Table 5 compares the fragment velocities obtained from test results processing with those obtained from the velocity target in the experiments. The velocity obtained from the velocity target for the 1# charge is significantly lower, and the velocity target did not capture the ideal maximum velocity of the fragment. For the 2# charge test, the fragment velocity obtained from the velocity target is less than the fragment velocities V_0 and V_{180} obtained from X-ray image processing, with an error of -7.44%. The velocity recorded by the velocity target in the 1# test is noticeably lower than $\overline{V}$. This discrepancy may be attributed to the fact that the lower-velocity fragments generated by the near-detonation end of the large aspect ratio hexagonal prism charge warhead, which detonated first, pass through the velocity target before the higher-velocity fragments do. There was a certain discrepancy between V_0

and V_{180}, mainly due to the angle between the axis of the test warhead specimen and the axis of the upper and lower X-ray tubes, which were not completely coplanar, resulting in inconsistent fragment velocities at 0° and 180° positions.

As evident from Table 5, the average velocities of fragments, determined via X-ray tests conducted on 1# and 2# test warhead specimens, exhibit a remarkable similarity, with a mere 3.84% discrepancy. Furthermore, the average fragment velocity ascertained from the 2# X-ray test aligns closely with the fragment velocity V_t measured by the velocity target, demonstrating minimal deviation. Consequently, this underscores the reasonableness and reliability of the measurement outcomes obtained through the X-ray tests presented in this paper.

Table 5. X-ray test results of hexagonal prism charge warhead specimens.

No.	Δt (μs)	V_t (m/s)	d	Fragment velocity(m/s)		$\bar{V}$ (m/s)	Error of V_t and $\bar{V}$
				V_0	V_{180}		
1#	1594	639.90	1.414375	1728.68	1761.76	1745.22	——
2#	691	1555.72	1.444375	1738.51	1622.94	1680.73	-7.44%

Note: Δt is the time interval of fragments passing through the velocity target; V_t is the fragment velocity measured by the target; d is the amplification ratio; $\bar{V}$ is the average of V_0 and V_{180}.

4.5 Simulation verification

Table 6 presents a comparison between the fragment velocities calculated through simulation (0.3 mm particle size) and those obtained from experiments. The errors between the fragment velocity V as calculated by simulation, and the fragment velocities V_0 and V_{180} of the 1# test warhead specimen, are -2.74 % and -0.88%, respectively, with an average error of -1.81%. For the 2# test warhead specimen, the errors between the simulation fragment velocity V and the fragment velocities V_0 and V_{180} are -2.19% and -8.69%, respectively, with an average error of -5.44%. These results verify the rationality of the simulation used in this study.

To further provide the basis for selecting 0.3 mm particle size in this study, based on the experimental data, we further compare the average errors of different particle size simulation calculations with the test results of 1# and 2#, as shown in Figure 15. Among them, the average errors of the simulation calculation results of 0.4 mm particle size and the test results of 1# and 2# were -2.86% and -6.45% respectively; the average errors of the simulation calculation results of 0.2 mm particle size and the test results of 1# and 2# were -3.77% and -7.32% respectively. Therefore, the accuracy of the simulation calculation results of 0.3 mm particle size is significantly better than 0.4 mm and 0.2 mm. Furthermore, the reduction in particle size leads to a significant reduction in computational efficiency.

Additionally, Figure 16 illustrates the comparison between the dispersion results of the hexagonal prism charge warhead shell fragments obtained from simulation and those obtained from X-ray tests. The outlines of the hexagonal prism shells at 25 μs and 40 μs, as determined by the simulation (0.3 mm particle size), align well with the outlines observed in the X-ray images from the experiments. The simulation model with a particle size of 0.5 mm has a significant difference between the flight profile simulation of the shell fragment and the profile obtained by the X-ray test. This study, under the premise of comprehensively considering the accuracy of fragment scattered morphology simulation, fragment velocity calculation accuracy, and calculation efficiency, selected 0.3 mm particle size as the particle size simulated in this study. The simulation calculation accuracy of this particle size and the shell scattered morphology simulation results were well verified by the experimental results.

Table 6. Comparison between experimental results and simulation results.

No.	Simulation V (m/s)	Test V_0 (m/s)	Error between V and V_0	Test V_{180} (m/s)	Error between V and V_{180}	Average error
1#	1777.35	1728.68	-2.74%	1761.76	-0.88%	-1.81%
2#		1738.51	-2.19%	1622.94	-8.69%	-5.44%

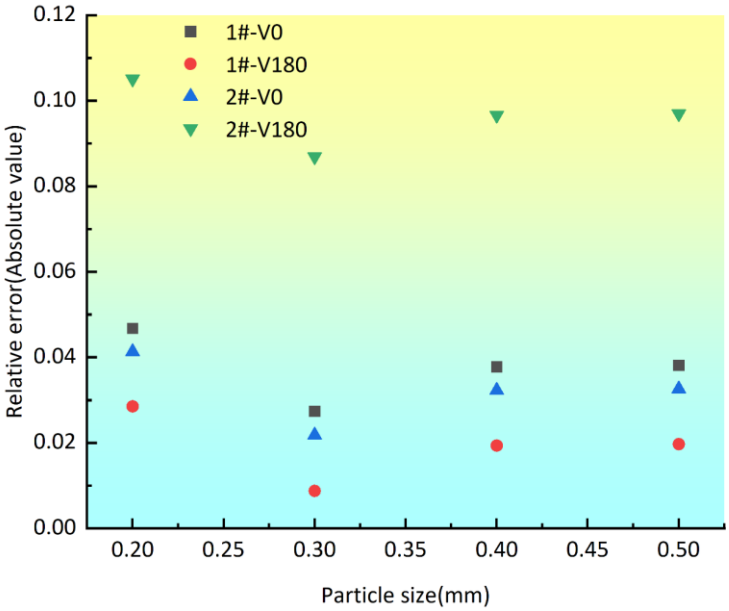

Figure 15. Particle size analysis.

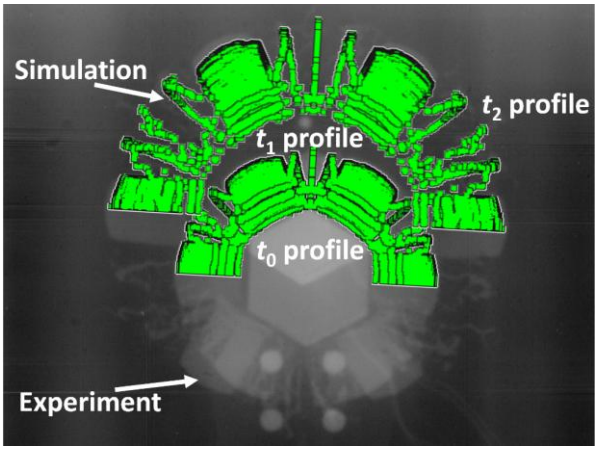

(a) 0.3 mm particle size

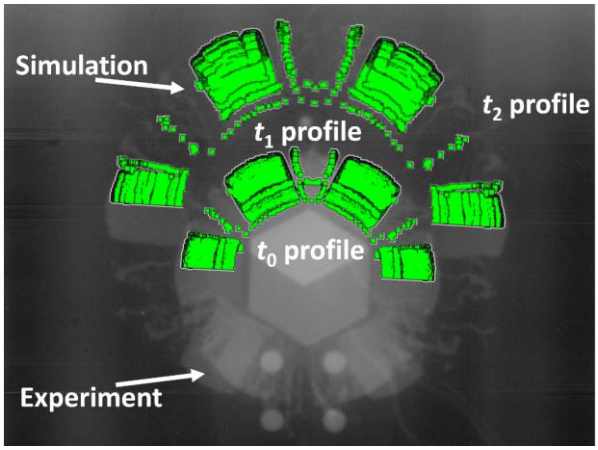

(b) 0.5 mm particle size

Figure 16. Comparison between simulation and test results.

4.6 Model verification

We compared the theoretical model with the experimental data. The calculation of the fragment velocity for the hexagonal prism charge warhead, as expressed by Eq. (25), and the maximum velocities derived from the processing of the 1# and 2# test results are illustrated in Figure 17. As depicted, the test velocities are situated close to the theoretical equation surface, indicating a high degree of conformity. The discrepancies between the theoretical velocities from Eq. (25) and the fragment velocities V_0 and V_{180} from the 1# test results are -0.67% and 1.23%, respectively. Similarly, the errors between the theoretical velocities from Eq. (25) and the fragment velocities V_0 and V_{180} from the 2# test results are 0.12% and -6.53%, respectively. These findings substantiate the strong agreement between the experimental results and Eq. (25), thereby validating the accuracy of the calculation model for the fragment velocity of the hexagonal prism charge warhead as established in this study.

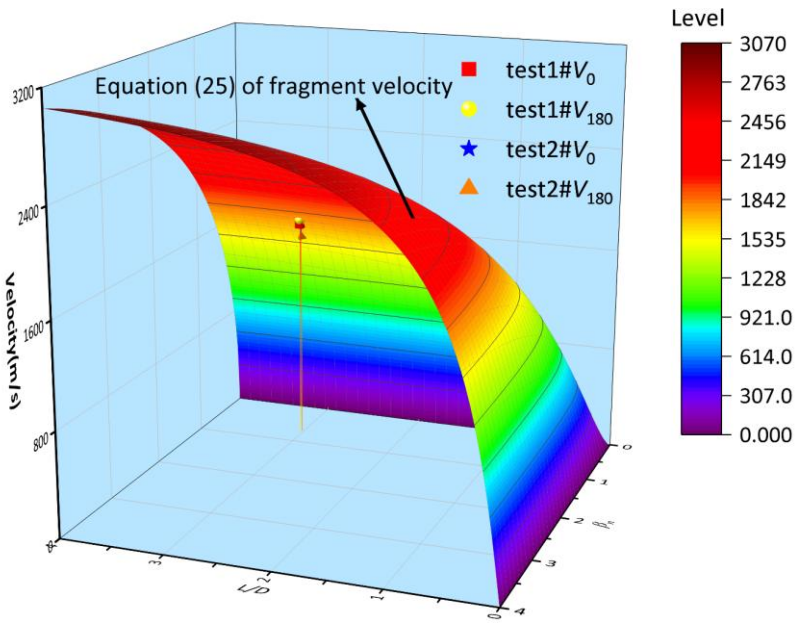

Figure 17. Comparison between the correction model and test results.

5 DISSCUSSION

5.1 Charge type

To ensure generality, hexagonal prism charge warheads of TNT charge were established with aspect ratios of 0.3, 0.6, 1.0, 2.0, 3.0, and 4.0. Aside from variations in charge types, all other structural dimensions were maintained consistent with the hexagonal prism charge warhead of the Comp-B explosive. Figure 18 illustrates a comparative analysis between the simulated velocities of these warheads and the predicted velocities derived from Eq. (25). Notably, the calculated velocities from the correction model align with the trend observed in the simulation velocities across different charge ratios. The discrepancies between these two sets of velocities gradually diminish as the aspect ratio increases. The maximum absolute error value, recorded at 7.64%, occurs near an aspect ratio of 0.3, while the minimum, at 2.35%, is observed near an aspect ratio of 3.0. This variation can be attributed to the axial rarefaction waves' influence on fragment velocity, which is more pronounced at lower aspect ratios and less significant at higher ones. Overall, the modified fragment v0elocity calculation model, excluding the rarefaction wave effect, demonstrates good agreement with the simulation data, with absolute error values remaining below 7.70%.

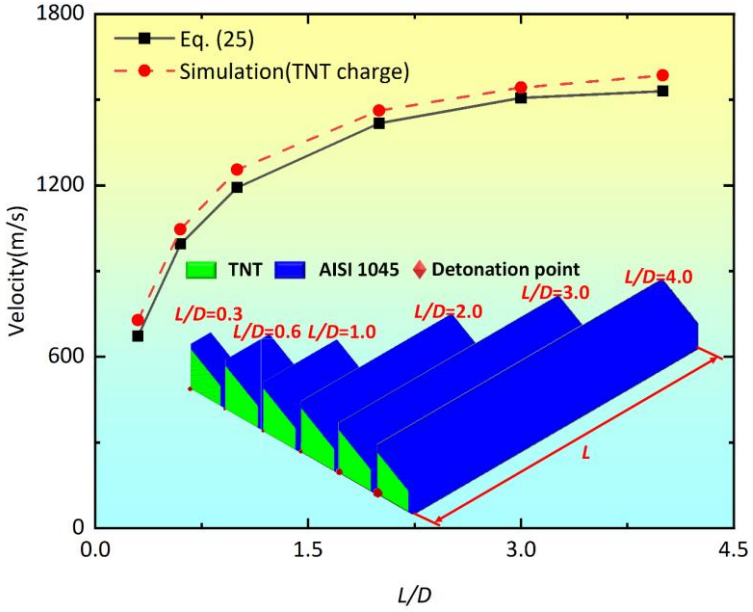

Figure 18. Comparison between the simulation and the predicted velocities.

5.2 Charge ratio

The charge diameter and shell thickness are key factors influencing the charge ratio β_n of a hexagonal prism charge warhead. To further validate the applicability of the fragment velocity calculation model established in Sections 2 and 3, variations in charge diameter were employed to manipulate the charge ratio β_n. Building upon Figure 2, the charge diameter D was sequentially altered to 20 mm, 30 mm, 40 mm, and 50 mm, maintaining a charge length of 50 mm and a shell thickness h of 2.6 mm, with all other model parameters held constant. Figure 19 illustrates a comparative analysis between the simulated fragment velocities of hexagonal prism charge warheads featuring these four distinct charge diameters and the predicted velocities derived from Eq. (25). There is a strong correlation between the simulated and predicted velocities, with the discrepancy diminishing as β_n increases. The maximum absolute error value recorded is 3.60%. Under conditions of a consistent charge configuration, discrepancies between simulated outcomes and predictions via Eq. (25) remain below 4.00%.

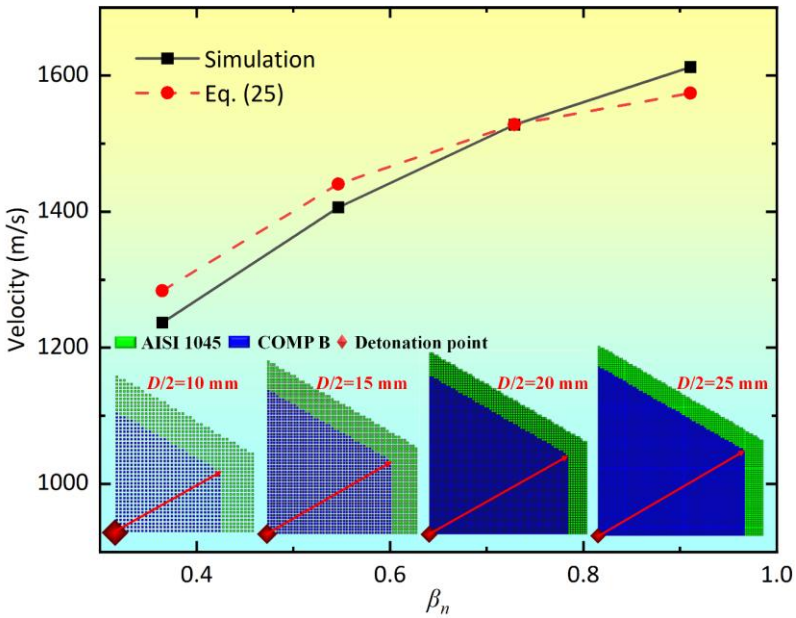

Figure 19. Result comparison under different charge ratios.

5.3 Polygonal applicability

To explore the applicability and accuracy of Eq. (23) for an n-sided polygon charge, the published literature data and simulation data were utilized to verify Eq. (23). Huang et al. (2023) carried out the static explosion test of the quadrangular prism charge warhead with a large aspect ratio. The radius of the outer circle of the charge was 24.75 mm, and the thickness of the shell was 2 mm. They obtained that the maximum velocity of the shell fragment initiating from the center of the end face was 2017.64 m/s based on the X-ray results shown in Figure 20. The maximum velocity of the fragment calculated by Eq. (23) was 2002.11 m/s, and the error between the theory and the experiment is -0.77%. Furthermore, in this study, the octagonal prism charge warhead model with a large aspect ratio was calculated using the SPH simulation method verified by experiments. The radius of the outer circle of the charge loading was 20 mm, and the shell thickness was 2.6 mm. We obtained the maximum velocity of the shell fragment initiated at the center of the end face, which was 1811.98 m/s, as shown in Figure 21. The maximum velocity of the fragments calculated by Eq. (23) was 1844.85 m/s, and the error between the theory and the experiment is -1.78%.

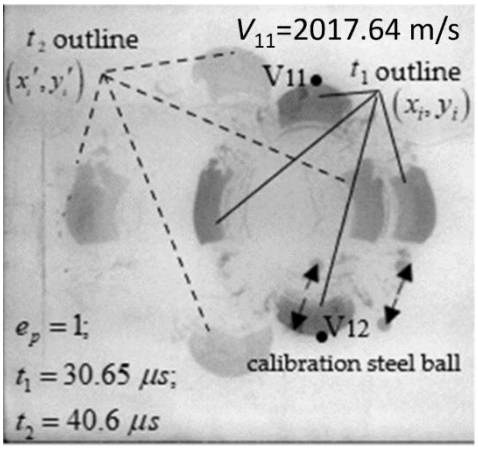

Figure 20. The test result of a quadrangular prism charge warhead (Huang et al. 2023).

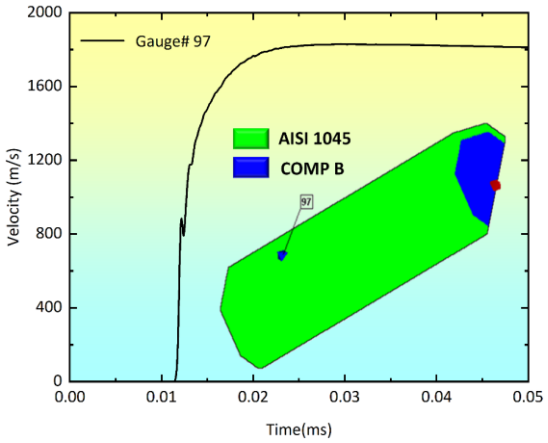

Figure 21. Simulation result of the fragment maximum velocity of an octagonal prism.

Furthermore, Guo et al. (2025) established a unified model for the fragment velocity of polygonal charges through dimensional analysis Eq. (23) was compared with Guo's Eq. (11), and the fragment velocity comparison curve shown in Figure 22 was obtained. It can be observed that, except for the triangular prism charge warhead, Eq. (23) is almost generally higher than Guo's Eq. (11), and the maximum absolute error value of Eq. (23) compared to Guo's Eq. (11) is 5.24%. However, Guo's Eq. (11) does not calculate the fragment maximum velocity of the charge, while Eq. (23) calculates the fragment maximum velocity of the charge. It can be foreseen that the error between the theoretical calculation value of Eq. (23) and the fragment maximum velocity of the actual polygonal charges will be further reduced. In addition, in the calculation of sandwich charges and cylindrical charges, Eq. (23) holds the highest accuracy.

In conclusion, the maximum velocity model of fragments established in this paper can be well adapted to polygonal charges, and the calculation results of the model are reasonable and reliable after verification by multiple types of data. Therefore, the model for calculating the fragment maximum velocity from sandwich charges to polygon charges and then to cylindrical charges is as follows:

$$V_M = \sqrt{2E}\sqrt{\frac{\beta_n}{(1+k/2)+\beta_n/3}} = \sqrt{2E}\sqrt{\frac{\beta_n}{\left[(\beta_n/6)^{\frac{n-2}{n-m}}+\frac{n-2}{n-m}\right]+\beta_n/3}} = \begin{cases} \sqrt{2E}\sqrt{\dfrac{\beta_n}{1+\beta_n/3}}\ (\text{Sandwich charge}) & n=2 \\ \sqrt{2E}\sqrt{\dfrac{\beta_n}{(\beta_n/6)^{1.41827}+1.41827+\beta_n/3}} & n\in\ *, (\beta_n = \dfrac{C_n}{nM_a}) \\ \sqrt{2E}\sqrt{\dfrac{\beta_n}{1+\beta_n/2}}\ (\text{Cylindrical charge}) & n=+\infty \end{cases} \quad (27)$$

Where C_n is the charge mass of the n-sided polygon charge.

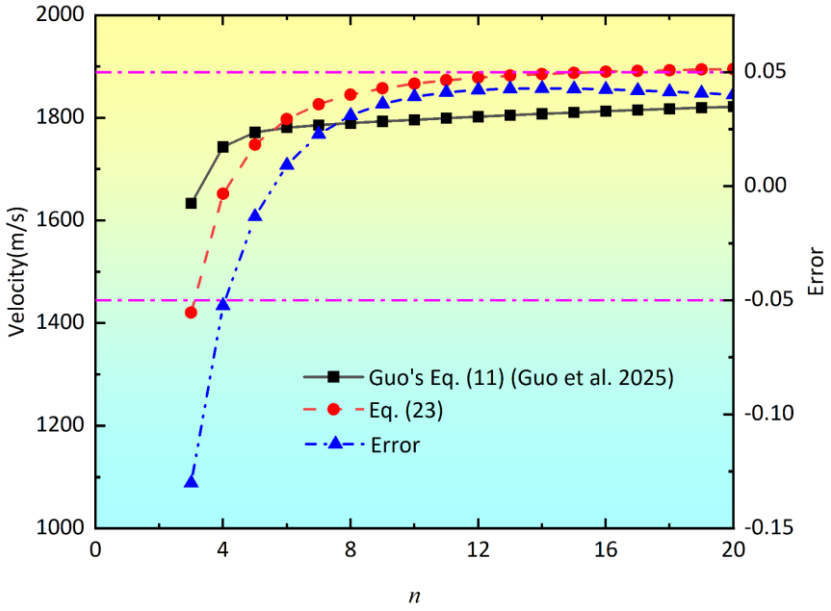

Figure 22. Comparison of calculation models for polygon fragment velocity.

6 CONCLUSION

In this paper, through a combination of theoretical analysis, numerical simulations, and experimental research, a new theoretical model for the fragment velocity of hexagonal prism charge warheads was established, and the influencing factors and variation laws of the fragment velocity were studied systematically. The following conclusions were drawn.

(1) A theoretical calculation model for the fragment velocity of the polygonal charge warhead was established. We propose a novel method to analyze the fragment velocity of polygonal charges using the sandwich charge and configuration decomposition method, which provides key insights for theoretical research on the fragment velocity of polygonal charges. Based on this method, a theoretical calculation model can be established to solve the fragment velocity of the polygonal charge warhead.

(2) The unknown quantities in the velocity calculation model were determined through the SPH method. The SPH method was used to determine the position of the maximum velocity of the axial fragment and the charge aspect ratio, which was almost unaffected by the rarefaction waves at the end. Based on the variation law of the maximum velocity of the fragment with the aspect ratio and the charge ratio obtained by simulation, the unknown quantities in the theoretical model of the fragment velocity calculation of the polygonal charge warhead were determined.

(3) The X-ray experiments conducted verified the accuracy of the simulation model and the established model of fragment velocity calculation. The maximum absolute error values of the experimental results and the simulation results and the established calculation model are 5.44% and 6.53%, respectively, and the fragment dispersion profile of the simulation is highly consistent with the X-ray profile taken by the experiment, proving the accuracy of the simulation and the established calculation model in this study.

(4) The applicability and prediction accuracy of the established computational model for different charge types, different charge ratios, and different polygonal charges are verified through a variety of data sources in the literature for simulation data, experimental data, and calculation formulas. The prediction accuracy of the polygon charge fragment velocity calculation model established in this study is controlled within 7.70%. This fully proves that the establishment of a computing model in this study is very accurate and applicable.

The research outcomes can provide a theoretical foundation for calculating the damage potential of the hexagonal prism charge warhead and its application in high-efficiency damage weapons. Additionally, it offers a valuable reference for the design, research, and application of other multi-surface structure warheads.

Acknowledgments:

This study was funded by the Opening Project of the State Key Laboratory of Explosion Science and Technology (Beijing Institute of Technology) [grant number KFJJ22-17M], the National Natural Science Foundation of China [grant number 12572213], and the Fundamental Research Funds for Central Universities [grant number D5000210576].

Author's Contributions: Conceptualization, Haokai Li and Yuan Li; Methodology, Haokai Li and Yuxiang Feng; Investigation, Haokai Li; Writing - original draft, Haokai Li; Writing - review & editing, Yuan Li; Funding acquisition, Yuan Li; Resources, Yuan Li; Supervision, Tao Suo.

Data Availability: Research data is only available upon request

Editor: Marcilio Alves

References

An X, Dong Y, Liu J, Tian C (2018) General formula to calculate the fragment velocity of warheads with hollow core. International Journal of Impact Engineering 113:1–8. https://doi.org/10.1016/j.ijimpeng.2017.11.006

Boswell GT, Rueb WG (1999) Flat-sided warhead

C D (2011) Release 14.0 documentation for ANSYS AUTODYN

Cullis IG, Dunsmore P, Harrison A, et al (2014) Numerical simulation of the natural fragmentation of explosively loaded thick walled cylinders. Defence Technology 10:198–210. https://doi.org/10.1016/j.dt.2014.06.003

Cunard DA, Thomas KA (1992) Programmable integrated ordnance suite (PIOS)

Deng H, Quan J, Liang Z (2022a) Influence of eccentric initiation on energy distribution gain of a warhead charge. Explosion And Shock Waves 42:3–15. https://doi.org/10.11883/bzycj-2021-0280

Deng X, Wu H, Yang X, et al (2022b) Preformed fragment velocity distribution of elliptical cross-section projectile. Lat Am j solids struct 19:e423. https://doi.org/10.1590/1679-78256835

Deng Y, Zhang X, Liu C, et al (2025) Investigation on fragment velocity distribution in elliptical cross-section warheads. Journal of Energetic Materials 1–30. https://doi.org/10.1080/07370652.2025.2495560

Deng Y, Zhang X, Xiao C, et al (2024) Experimental study on fragments dispersion characteristics of elliptical cross-section casing under explosive loading. Thin-Walled Structures 197:111601. https://doi.org/10.1016/j.tws.2024.111601

Dhote KD, Murthy KPS, Rajan KM, Mahesh M Sucheendran (2015) Directional warhead design methodology for a tailored fragment beam. Central European Journal of Energetic Materials 12:637–649

Ding L, Li Z, Liang M, et al (2017) The dispersion rule of fragments about the asymmetric shell. Shock and Vibration 2017:9810978. https://doi.org/10.1155/2017/9810978

Feng S, Huang G, Dong Y (2009) A new design method of fragment focusing warhead. Journal of Ballistics 21:24–26, 38

Gao Y, Feng S, Xiao X, et al (2023) Fragment characteristics from a cylindrical casing constrained at one end. International Journal of Mechanical Sciences 248:108186. https://doi.org/10.1016/j.ijmecsci.2023.108186

Gao Y, Zhang B, Yan X, et al (2020) Axial distribution of fragment velocities from cylindrical casing with air parts at two ends. International Journal of Impact Engineering 140:103535. https://doi.org/10.1016/j.ijimpeng.2020.103535

Gao YG, Feng SS, Zhang B, Zhou T (2019) Effect of the length-diameter ratio on the initial fragment velocity of cylindrical casing. IOP Conf Ser: Mater Sci Eng 629:012020. https://doi.org/10.1088/1757-899X/629/1/012020

Grisaro H, Dancygier AN (2015) Numerical study of velocity distribution of fragments caused by explosion of a cylindrical cased charge. International Journal of Impact Engineering 86:1–12. https://doi.org/10.1016/j.ijimpeng.2015.06.024

Guo Y, Li Y, Li H, Suo T (2025) Unified formula for fragment velocity of polygonal charges. International Journal of Impact Engineering 202:105296. https://doi.org/10.1016/j.ijimpeng.2025.105296

Guo Z, Huang G, Chen P, et al (2023) Fragments dispersion characteristics of the casing with the mismatched shell under internal explosive loading. International Journal of Impact Engineering 171:104370. https://doi.org/10.1016/j.ijimpeng.2022.104370

Guo Z, Huang G, Liu C, Feng S (2018) Velocity axial distribution of fragments from non-cylindrical symmetry explosive-filled casing. International Journal of Impact Engineering 118:1–10. https://doi.org/10.1016/j.ijimpeng.2018.03.011

Guo Z, Huang G, Liu H, Feng S (2020) Fragment velocity distribution of the bottom part of d-shaped casings under eccentric initiation. International Journal of Impact Engineering 144:103649. https://doi.org/10.1016/j.ijimpeng.2020.103649

Guo Z, Huang G, Zhu W, et al (2019a) Mechanism and suppression of the effect of axial rarefaction waves on the eccentric initiation effect. International Journal of Impact Engineering 124:37–47. https://doi.org/10.1016/j.ijimpeng.2018.10.009

Guo Z, Huang G, Zhu W, Feng S (2019b) Fragment velocity distribution of D-shaped casing with multiple fragment layers. International Journal of Impact Engineering 131:85–93. https://doi.org/10.1016/j.ijimpeng.2019.04.027

Gurney RW (1943) The initial velocities of fragments from bombs, shell, and grenades

Hamada T, Itoh S, Kato H (2004) An investigation on overdriven detonation phenomenon in concentric double cylindrical high explosive. Materials Science Forum 465–466:379–384. https://doi.org/10.4028/www.scientific.net/MSF.465466.379

Held M (2001) Velocity enhanced warheads. Journal of explosives and propellants ROC(Taiwan) 17:1–12

Hu H, Xiao C (2019) Array explosion——a conventional high efficiency damage technology. Chinese Journal of Energetic Materials 27:717–719. https://doi.org/10.11943/CJEM2019098

Huang G, Li W, Feng S (2015) Axial distribution of fragment velocities from cylindrical casing under explosive loading. International Journal of Impact Engineering 76:20–27. https://doi.org/10.1016/j.ijimpeng.2014.08.007

Huang X, Zhang Y, Liu H, et al (2023) Dispersion properties of fragments of square metal shells driven by explosive loading. Lat Am j solids struct 20:e511. https://doi.org/10.1590/1679-78257833

Jin K, Li P, Wu Q, Jin X (2004) Numerical simulation on acceleration process of flyer driven by detonation product through an air cushion. Explosion And Shock Waves 24:419–424. https://doi.org/1001-1455(2004)05-0419-06

Johnson GR (1983) A constitutive model and data for metals subjected to large strains, high strain rates and high temperatures. The Hague, Netherlands

Jones GE, Kennedy JE, Bertholf LD (1980) Ballistics calculations of R. W. Gurney. American Journal of Physics 48:264–269. https://doi.org/10.1119/1.12135

Karpp RR, Predebon WW (1975) Calculations of fragment velocities from naturally fragmenting munitions

Kennedy DR (1999) A historical review of aimable air defense warhead technology. San Antonio, TX, USA, pp 618–625

Kong X, Wu W, Li J, et al (2013) A numerical investigation on explosive fragmentation of metal casing using Smoothed Particle Hydrodynamic method. Materials & Design 51:729–741. https://doi.org/10.1016/j.matdes.2013.04.041

Li H, Feng Y, Li Y, Suo T (2024a) Power characteristics of drum-shaped warheads under multi-point detonations. Explosion And Shock Waves 44:40–51. https://doi.org/10.11883/bzycj-2023-0317

Li Y (2016) Study on theories and technologies of asymmetrically initiated warhead. Beijing Institute of Technology

Li Y, Guo Y, Wen Y, et al (2024b) Methods for obtaining the actual radial distribution of the fragment velocity through X-ray photography. Measurement 234:114848. https://doi.org/10.1016/j.measurement.2024.114848

Li Y, Li X, Wen Y, Suo T (2023a) Detonation driving rules for cylindrical casings under asymmetrical multipoint initiations. Defence Technology 23:35–49. https://doi.org/10.1016/j.dt.2022.10.001

Li Y, Ren T, Wen Y, Suo T (2023b) Impact of aspect ratio on fragment velocity distribution for hollow charges. Materials & Design 228:111815. https://doi.org/10.1016/j.matdes.2023.111815

Li Y, Wen Y (2014) Simulation on damage effectiveness of hexagonal prism aimable warhead with multi-point synchronous initiations. Journal of Beijing Institute of Technology 23:1–7

Li Y, Wen Y (2017) Experiment and numerical modeling of asymmetrically initiated hexagonal prism warhead. Advances in Mechanical Engineering 9:1687814016687966. https://doi.org/10.1177/1687814016687966

Li Y, Yu C, Suo T, Wen Y (2023c) Maximum fragment velocity of hollow charges with different aspect ratios. International Journal of Impact Engineering 178:104622. https://doi.org/10.1016/j.ijimpeng.2023.104622

Liao W, Jiang J, Men J, et al (2021) Effect of the end cap on the fragment velocity distribution of a cylindrical cased charge. Defence Technology 17:1052–1061. https://doi.org/10.1016/j.dt.2020.06.024

Lim S (2013) Acceleration profile of a flat flyer driven by detonation isentrope. Propellants, Explosives, Pyrotechnics 38:410–418. https://doi.org/10.1002/prep.201200188

Ling Q, He Y, He Y, Zhou J (2017) Numerical simulation of directed scattering of fragments driven by sector-shaped double-layer charge. Chinese Journal of High Pressure Physics 31:557–565. https://doi.org/10.11858/gywlxb.2017.05.008

Liu H, Huang GY, Guo ZW, Feng SS (2022) Fragments velocity distribution and estimating method of thin-walled cylindrical improvised explosive devices with different length-to-diameter ratios. Thin-Walled Structures 175:109212. https://doi.org/10.1016/j.tws.2022.109212

Ma T, Shi X, Li J, Ning J (2020) Fragment spatial distribution of prismatic casing under internal explosive loading. Defence Technology 16:910–921. https://doi.org/10.1016/j.dt.2019.11.006

Mott NF (1947) Fragmentation of shell cases. Proceedings of the Royal Society of London Series A Mathematical and physical sciences 189:300–308. https://doi.org/10.1098/rspa.1947.0042

Ning JG, Duan Y, Xu XZ, Ren HL (2017) Velocity characteristics of fragments from prismatic casing under internal explosive loading. International Journal of Impact Engineering 109:29–38. https://doi.org/10.1016/j.ijimpeng.2017.05.018

Ramudu BV, Reddy CJ, Madhu V (2019) Flash X-ray radiography technique to study the high velocity impact of soft projectile on E-glass/epoxy composite material. Defence Technology 15:216–226. https://doi.org/10.1016/j.dt.2018.08.014

Resnyansky AD, Wildegger-Gaissmaier AE, Katselis G (1999) Directional fragmentation warheads: a theoretical and experimental investigation (English). San Antonio, Texas, pp 543–550

Shi Y, Tong Zhou, Guo Z, et al (2023) Velocity distribution of preformed fragments from concave quadrangular charge structures. International Journal of Impact Engineering 176:104551. https://doi.org/10.1016/j.ijimpeng.2023.104551

Taylor GI (1963) The fragmentation of tubular bombs. Advisory Council on Scientific Research and Technical Development 5:202–320

Terry NB, Cone PP (2020) Hypersonic technology. Strategic Studies Quarterly 14:74–99

Waggener S (2001) Relative performance of anti-air missile warheads. Interlaken, Switzerland

Wang G, Yin T, Cao Y (2022a) Research on the development of foreign hypersonic offensive and defensive weapons. Modern Defense Technology 50:26–32. https://doi.org/10.3969/j.issn.1009-086x.2022.02.004

Wang H, Xie J, Ji L (2022b) Progress and development trend of efficient damage technology. Foresight Science and Technology 1:113–124. https://doi.org/10.3981/j.issn.2097-0781.2022.04.008

Wang J, Hu D, Tang Y, et al (2023) Design and numerical simulation of charge curve of focusing warhead. J Phys: Conf Ser 2478:112025. https://doi.org/10.1088/1742-6596/2478/11/112025

Wang L, Han F, Chen F (2016) Fragment velocity distribution of velocity enhanced warhead under double symmetric initiations. Propellants Explo Pyrotec 41:672–681. https://doi.org/10.1002/prep.201500234

Wang SS (2019) Terminal effects, 2nd ed. Science Press, Beijing

Ye P, Dong YX, Sun QT, et al (2024) Double casing warhead with sandwiched charge: The axial distribution of fragments velocities. Defence Technology 34:201–216. https://doi.org/10.1016/j.dt.2023.12.014

Zhang BP, Zhang QM, Huang FL (2001) Detonation physics. Weapons Industry Press, Beijing

Zhang Q, Jian H, Zheng G, et al (2023) The interaction of detonation waves by multipoint initiation under small-size charge condition. Physics of Fluids 35:117105. https://doi.org/10.1063/5.0171312

Zhang X, Huang H, Qiao L (2011) Detonation wave propagation in double-layer cylindrical high explosive charges. Propellants, Explosives, Pyrotechnics 36:197–293. https://doi.org/0.1002/prep.201000004

Zhao Y, Li J, Ma T (2016a) Experiment on spread processes of the spreadable aimed warhead. Chinese Journal of High Pressure Physics 30:116–122. https://doi.org/10.11858/gywlxb.2016.02.005

Zhao Y, Ma T, Li J, Ning J (2016b) Study on dynamic response of multi-body structure under explosive driving. Sci China Technol Sci 59:1360–1369. https://doi.org/10.1007/s11431-016-0263-4

(2001) US-UK program studies directional warhead technology. Jane's Missiles & Rockets 5